

Article

Nanomechanical, Structural and Electrochemical Investigation of Amorphous and Crystalline MoO₃ Thin-Film Cathodes in Rechargeable Li-Ion Batteries

Wissem Methani ^{1,2}, Edit Pál ¹, Sándor Lipcsei ³ , Dávid Ugi ³ , Zoltán Pászti ¹, István Groma ³, Péter Jenei ³, Zoltán Dankházi ³  and Robert Kun ^{1,2,*} 

- ¹ Research Centre for Natural Sciences, Institute of Materials and Environmental Chemistry, Magyar Tudósok Körútja 2, 1117 Budapest, Hungary; methaniw0@gmail.com (W.M.); pal.edit@ttk.hu (E.P.); paszti.zoltan@ttk.hu (Z.P.)
- ² Department of Chemical and Environmental Process, Faculty of Chemical Technology and Biotechnology, Budapest University of Technology and Economics, Műegyetem Rakpart 3, 1111 Budapest, Hungary
- ³ Department of Materials Physics, Eötvös Lóránd University, Pázmány Péter Sétány 1/a, 1117 Budapest, Hungary; lipcseiandor98@gmail.com (S.L.); david.ugi@ttk.elte.hu (D.U.); groma@metal.elte.hu (I.G.); jenei.peter@ttk.elte.hu (P.J.); zoltan.dankhazi@ttk.elte.hu (Z.D.)
- * Correspondence: kun.robert@ttk.hu; Tel.: +36-1-382-6579



Citation: Methani, W.; Pál, E.; Lipcsei, S.; Ugi, D.; Pászti, Z.; Groma, I.; Jenei, P.; Dankházi, Z.; Kun, R. Nanomechanical, Structural and Electrochemical Investigation of Amorphous and Crystalline MoO₃ Thin-Film Cathodes in Rechargeable Li-Ion Batteries. *Batteries* **2022**, *8*, 80. <https://doi.org/10.3390/batteries8080080>

Academic Editor: Claudio Gerbaldi

Received: 27 June 2022

Accepted: 22 July 2022

Published: 28 July 2022

Publisher's Note: MDPI stays neutral with regard to jurisdictional claims in published maps and institutional affiliations.



Copyright: © 2022 by the authors. Licensee MDPI, Basel, Switzerland. This article is an open access article distributed under the terms and conditions of the Creative Commons Attribution (CC BY) license (<https://creativecommons.org/licenses/by/4.0/>).

Abstract: In this work, a comprehensive investigation of amorphous and crystalline modification of identical electrode active material as a thin-film electrode for a future all-solid-state Li-ion battery application is presented and discussed. Using the proposed micro-battery system, we aim to unravel the effect of the crystallinity of the positive electrode material on the intrinsic durability of all-solid-state thin-film Li-ion batteries during prolonged electrochemical cycling. We demonstrate the preparation, structural-, nanomechanical and electrochemical characteristics of molybdenum (VI) oxide (MoO₃) thin-film cathodes based on their different crystallinity. The nanomechanical properties of the electrode layers were determined using nanoindentation along with acoustic emission studies. Based on the electrochemical test results, as-prepared thin films that did not go under any heat treatment showed the best performance and stability throughout cycling around 50 μAh initial capacity when cycled at C/2. This suits well their nanomechanical properties, which showed the highest hardness but also the highest flexibility in comparison with the heat-treated layers with lower hardness, high brittleness, and numerous cracks upon mechanical loads. According to our results, we state that amorphous-type electrode materials are more durable against electro-chemo-mechanical-aging related battery performance loss in all-solid-state Li-ion batteries compared to their crystalline counterparts.

Keywords: Li-ion battery; thin-film battery sputtering; amorphous cathode; electrochemical performance; impedance spectroscopy; X-ray line profile analysis; nanoindentation; acoustic emission

1. Introduction

During the past few decades, the demand for portable power has been steadily increasing; this is due to the increasing demand for mobile handheld devices (cellular phones, tablets, laptops, “smart” electronic devices, etc.), electric vehicles, such as hybrid EV and battery electric vehicles (BEV), aerospace applications, etc. The conditions of usage of these batteries may differ based on the applications. Thus, environment protection, manufacturing cost, the safety of these storage devices, and sufficient autonomy for reduced weight and size are essential points for all these new technologies, particularly in the field of rechargeable batteries. Thin metal-oxide films have long been recognized as promising materials for battery electrodes. Thin-film electrodes can enable active materials with low conductivity to improve their electro-chemical characteristics. It is possible to lower the thickness of thin films to a point where the electrochemical behavior is not significantly

influenced by electrical conductivity [1]. There are several methods that have already been successfully applied for the fabrication of thin-film electrodes, such as ion beam sputtering [2], pulsed laser deposition (PLD) [3], the sol–gel method [4], spray coating [5], flash evaporation [6], electrochemical deposition [7], radio frequency (RF) sputtering [8], flame spray pyrolysis (FSP) [9], etc. Among the above thin film deposition techniques, direct current (DC) sputtering is an attractive method for the preparation of thin-film metals due to the target's high conductivity. In fact, sputtered metal oxide thin layers are rather amorphous in nature. Regarding the battery performance, authors claim that polycrystalline electrode materials are required for excellent electrochemical performance [10]. In crystalline materials, the electrochemical performances are conditioned by the structural stability, crystal orientation, defects in crystals, the stoichiometric limitation of ion insertion, the available energetically equivalent sites for ion transport, phase transition, etc. [11]. In most cases, in order to achieve polycrystalline thin films, the as-prepared (and thereby amorphous) layers have to be post-heat treated or synthesized at elevated temperatures ($>500\text{ }^{\circ}\text{C}$) [12]. Nevertheless, the high-temperature annealing step often results in undesirable interphase formation [13] and does not allow for the application of heat sensitive and mechanically flexible, e.g., polymeric substrates, nor allow the fabrication of battery cell stacks (repeating units of sequentially deposited single battery cells connected with each other) for the increased areal energy density. There are several reasons to use amorphous material instead of their crystalline counterparts [14–16]. Amorphous materials possess higher kinetics of ionic intercalation and deintercalation; there is no directionality in the Li-ion transport, i.e., lithium diffusion is isotropic [17]; they have larger free volume and more interstitial sites in their structures, thereby having enhanced storage capacities [18–21]; and they can buffer electrochemical lithiation induced mechanical stress.

Crystalline molybdenum(VI) oxide (MoO_3) has been tested as an electroactive compound in rechargeable Li-ion batteries earlier [22–25]. Its advantages are the high theoretical capacity (372 mAh/g) when a two-electron reaction is exploited, (for a- MoO_3 : $Q_N = 279\text{ mAh/g}$, at 1.5 moles Li^+/MoO_3 and $Q_N = 186\text{ mAh/g}$ for 1 moles Li^+/MoO_3) and easy processing as thin films. The amorphous-to-crystalline transition of MoO_3 thin layers proceeds at relatively mild temperatures of $T \sim 300\text{ }^{\circ}\text{C}$ [26] (for LiCoO_2 and LiMn_2O_4 at $T \sim 600$ to $700\text{ }^{\circ}\text{C}$), which makes this a very suitable candidate to investigate in SSBs based on amorphous, as well as crystalline electrodes. Thereby, using a MoO_3 -positive electrode, the detailed investigation of the electrochemical performance regarding the amorphous vs. crystalline form of the same material can be carried out easily. To our knowledge, there are only a few publications on the comparison of the electrochemical properties of MoO_3 in amorphous and crystalline forms. Julien et al. [27] investigated flash-evaporated MoO_3 thin films for cathode materials with different crystalline structures, i.e., amorphous a- MoO_3 and polycrystalline monoclinic–orthorhombic mixed phase MoO_3 and orthorhombic MoO_3 . It was stated that the ionic transport was weaker in the disordered phases; although, the cell voltage remained high. They found similar results in the case of sputtered MoO_3 thin films in organic liquid electrolyte cells, i.e., the ionic transport was strongly dependent on the film crystallinity [28].

The current study focuses on the comprehensive investigation of the structural and electrochemical performance of amorphous and partially crystalline MoO_3 thin film electrodes in rechargeable Li-ion batteries. Nanomechanical characteristics, and acoustic emission behaviors of the MoO_3 -based layers along with their crystallinity are discussed. The as-sputtered and post-heat treated MoO_3 electrodes were assembled into coin cells, then, electrochemical performance, such as capacity, capacity retention, and power density characteristics were analyzed. The correlation between the layer's crystallinity and its electrochemical properties was determined.

2. Experimental

2.1. Preparation Method

MoO_3 thin layers were prepared by the DC sputter deposition technique. The thin layers were deposited onto Al substrates using a molybdenum target (Lesker, K.J.) with a constant gas flow of 30 sccm argon and 10 sccm oxygen, a deposition pressure of 1.10^{-1} Pa at a DC power of 200 W. To have crystalline MoO_3 layers, the as-sputtered samples were heat treated at 200 °C and 300 °C for 1 h with a heating rate of 10 °C/min in air, respectively. For electrochemical testing, 14 mm diameter discs of the MoO_3 layers were used as the positive electrodes, 1 M LiPF_6 in ethylene carbonate and diethyl carbonate (EC/DEC) 50/50 (*v/v*) was used as the electrolyte (Sigma Aldrich, St. Louis, MO, USA), and metallic lithium foil as counter electrode 16 mm in a CR2032 type coin cell and a Whatman glass fiber separator 18 mm. The battery cells were assembled in an argon-filled glove box (O_2 and H_2O levels < 0.1 ppm).

2.2. Characterization Methods

- X-ray photoelectron spectroscopy (XPS)

The XPS analyses were performed by using an Omicron EA 125 electron spectrometer (Omicron NanoTechnology GmbH, Taunusstein, Germany) in the “Fixed Analyzer Transmission” mode; photoelectrons were excited by non-monochromatized $\text{MgK}\alpha$ (1253.6 eV) radiation. The energy scale of the electron spectrometer was calibrated according to the ISO 15472 standard. The estimated uncertainty of the binding energies obtained in this work is around ± 0.2 eV. Samples were investigated in their “as received” state, without any cleaning in solvents. High-resolution spectra were obtained from the regions of interest using a “pass energy” of 30 eV, providing resolution around 1 eV. Spectra were processed with the CasaXPS package (Casa Software Ltd., v.2.3.12, Teignmouth, UK) [29], while quantitative evaluation of the data was performed with the XPSMultiQuant package (M. Mohai, v.7.00, Budapest, Hungary) [30], during which a homogeneous depth distribution was assumed for all components. As the line shape of the Mo 3d spin-orbit doublet suggested the almost exclusive presence of the Mo^{6+} ionic state, the referencing of the binding energy scale was possible by setting the maximum of the Mo 3d_{5/2} peak to 232.5 eV, which is the binding energy reported for Mo^{6+} ions in MoO_3 [31,32]. This correction was confirmed by the resulting C 1s binding energy slightly below 285 eV.

- X-ray line profile analysis

The crystallinity of the layers was investigated by X-ray diffraction (RIGAKU SMART-LAB diffractometer, Tokyo, Japan) in Bragg–Brentano geometry using Cu K- α and K- β radiation. The crystallinity of the samples is defined by the ratio between the total sample intensity and the intensity of the crystalline phase peaks, namely,

$$c = \frac{I_{\text{crystalline}}}{(I_{\text{crystalline}} + I_{\text{amorphous}})} \quad (1)$$

The steps to obtain the crystallinity consisted of deduction of constant background, a rough linear fitting of amorphous phase, integration of different phases via Simpson method, and lastly calculating the crystallinity. In the case of crystalline layers, a clear, good quality reflection (i.e., without overlapping with other peaks) was selected and scanned with monochromatized K- α radiation in grazing angle. Afterward, by analyzing the X-ray line profile with the so-called restricted moments method developed by Groma et. al. [33,34], the average dislocation density and average grain size were determined. From the asymptotic behavior of k th order restricted moments

$$V_k = \frac{\int q^k I(q) dq}{\int I(q) dq} \quad (2)$$

of the measured $I(q)$ X-ray intensity distribution, one may obtain

$$v_2 = \frac{2}{\pi^2 d} q + \frac{\langle \rho^* \rangle}{2\pi^2} \ln\left(\frac{q}{q_0}\right) \quad (3)$$

and second order and fourth order restricted moments, respectively. In the above equation,

$$q = \frac{2}{\lambda} (\sin(\Theta) - \sin(\Theta_0)) \quad (4)$$

is the diffraction distance, where θ_0 is the exact Bragg-angle and λ is the wavelength of the applied X-ray radiation. One can clearly see that both the average dislocation density ($\langle \rho^* \rangle$) and average grain size ($1/d$) appear in the second and fourth-order restricted moments, which means that one can determine these parameters by subtracting the appropriate background and fitting the restricted moments [35].

- Nanoindentation

To investigate the mechanical properties of MoO₃-bearing layers, a custom-made nano indenter was used [36,37]. The developed apparatus is suitable for the investigation of the nano deformation methods by its fast response speed and mountable acoustic emission (AE) sensor, besides the crucial mechanical properties. An AE signal could form during plastic events, such as crack formation and crack propagation, cooperative dislocation movements, and different types of phase transformations [38]. The detection of AE is based on the elastic energy release due to the irreversible change in the specimen's (micro)structure. Near the AE source, the released energy forms a stress pulse, which propagates through the material. The elastic stress wave component, which is perpendicular to the surface, is detected by piezoelectric transducers, which are coupled to the specimen's surface mechanically [39]. For the nanoindentation analyses, a diamond Berkovich-type indenter tip was used. The accuracy of the depth and load measurements were 1 nm and 1 μ N, respectively, and the applied sampling rate was 200 Hz. In this indentation measurement, there was no applied load or strain control to avoid the artificial effects of the electrical feedback. The spring attached platen velocity was set to a constant value to carry out the tip penetration, which was proportionate to the average indentation rate. In the case of AE measurements, the sampling rate of the data streaming was 2 MHz (adjusted to the known main signal frequency of 50–500 kHz). The signal detection threshold set to 0.01 mV was remarkably over the noise level.

- Scanning electron microscopy (SEM)

Morphological and microstructural characterizations of the thin layers were carried out with focused ion beam/scanning electron microscopy (FIB-SEM) system using FEI Quanta 3D dual beam scanning electron microscope. The as-prepared, heat treated at 200 °C and 300 °C layers were analyzed pre and post-nanoindentation in order to visually inspect the indentation effect on the layers and their patterns.

- Electrochemical tests

The assembled battery cells were cycled between 1 and 3.5 V under galvanostatic conditions using a Biologic VMP-300 electrochemical workstation. The initial 10 cycles were performed at a rate of C/2, followed by long-term cycling at 10C for an additional 500 full cycles.

2.3. Results and Discussion

(1) Chemical and crystallographic characterizations

Chemical composition including the Mo:O atomic ratio of the as-sputtered and the annealed thin films were characterized by XPS. Results of the quantitative analysis are presented in Table 1. All examined surfaces contain a relatively high amount of carbon. As even a minimal in situ ion bombardment very significantly decreased the carbon

content, it was assigned to surface hydrocarbon contamination adsorbed from ambient air. Indeed, the binding energy of the main C 1s peak around 284.8 eV is characteristic of hydrocarbon contamination.

Table 1. Summary of the XPS data for the as-prepared and heat-treated samples.

Sample	C % (at%)	O% (at%)	Mo% (at%)	Mo:O Ratio
as-sputtered	32.5	45.3	17.4	1:2.60
200 °C	21.6	55.4	21.6	1:2.56
300 °C	31.1	48.1	19.6	1:2.45

Figure 1 shows the detailed Mo 3d spectra of the three samples. Most of the Mo 3d signals are assigned to the $3d_{5/2}-3d_{3/2}$ spin-orbit doublet of the Mo^{6+} ions ($3d_{5/2}$ component at 232.5 eV binding energy). The width of the Mo^{6+} peaks clearly decreased with increasing annealing temperature (full width at half maximum of the Mo^{6+} $3d_{5/2}$ peak was 1.54 eV, 1.44 eV, and 1.23 eV for the untreated, 200 °C, and 300 °C annealed samples, respectively). This suggests a more uniform, ordered local environment for the Mo ions in films annealed at higher temperatures. At the same time, a slight asymmetry at the low-binding energy side of the main peaks indicated the presence of another chemical state, which was slightly more pronounced in the 300 °C sample. It was modeled by a second spin-orbit doublet, which accounted for roughly 4–5% of the total Mo signal in the untreated and the 200 °C annealed sample and 7% in the 300 °C sample. According to its $3d^{5/2}$ binding energy around 231 eV, it was assigned to Mo^{5+} ions [31].

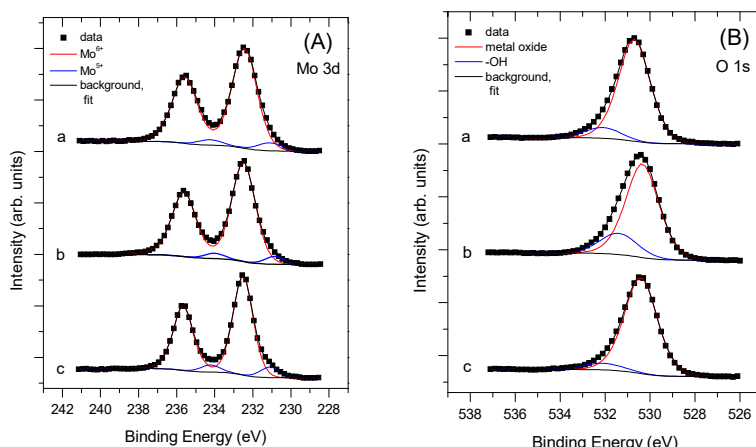


Figure 1. Panel (A): Mo 3d and Panel (B): O 1s spectra of the untreated (a), 200 °C (b), and 300 °C (c) annealed sputtered Mo-oxide films.

The O 1s spectra of the samples were rather similar; they were dominated by a peak at 530.4–530.6 eV arising from lattice oxygen in Mo-oxide, while a weak component at its high binding energy side contained contributions from surface hydroxyl groups as well as from carbon-bound oxygen atoms belonging to the carbonaceous contamination. All surfaces were somewhat oxygen-deficient. The Mo:O ratio in the untreated sample was 1:2.60, which hardly changed in the 200 °C-treated sample but decreased below 1:2.50 in the 300 °C sample. The results of the XPS investigations suggest that our cathode material consists of MoO_3 with a Mo:O ratio close to 1:3; although, some variation in the microstructure is expected as a consequence of the annealing.

To reveal the crystallographic features of the as-sputtered and the annealed MoO_3 thin films, XRD measurements were carried out. The diffractogram measured in Bragg–Brentano geometry of the as-sputtered MoO_3 thin film does not present any peaks, meaning the layer is completely amorphous (*cf.* Figure 2a). When heat treated at 200 °C, the layer still presents its amorphous features, while crystallization only took place when the layers were heated

to 300 °C. The diffractograms of the thin films grown on aluminum substrate show the orthorhombic α phase of MoO₃ referred to with a delta symbol; however, impurities (namely, multiple AlO_x phases) referred to with a star symbol are also observed. The appearance of the AlO_x phases can be attributed to the conventional heat treatment procedure.

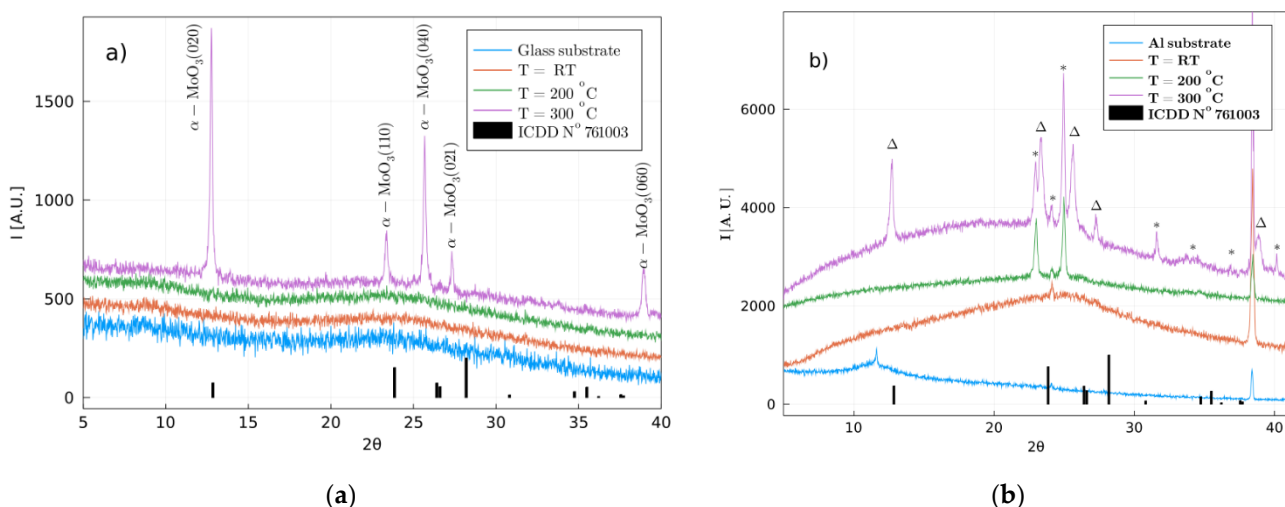


Figure 2. (a) XRD patterns of MoO₃ sputtered on aluminum substrate (Δ : orthorhombic α -MoO₃, *: Al-oxides), (b) crystallinity was estimated with the presented numerical procedure. The peak positions were given manually, the fitting is linear. The blue line is the original sample diffractogram, the orange one is the amorphous background, and the green is the studied crystalline phase.

As was stated earlier, the calculation of the grade of the crystallinity of the thin layers before and after annealing was made in an approximate but simple manner, which is useful for the analysis of Bragg–Brentano data with multiple peaks. The fluctuating background (BG) was fitted via a two-point linear fitting, while the peak intervals were left out, via linear bridging (see Figure 2). Afterward, the amorphous background was subtracted from the whole diffractogram, obtaining the diffraction peaks corresponding to only the crystalline MoO₃- α phase. In the next step, the original diffractogram and the crystalline phases were integrated via the Simpson method. The samples annealed below 300 °C had a rather amorphous character, they were 0% crystalline; however, those that were heated to 300 °C exhibited 5.4% crystallinity on the aluminum substrate. The low crystalline character in the case of the samples processed and deposited onto the aluminum substrate could be explained by the appearance of AlO_x phase impurities, which could have had a pinning effect on the growth of MoO₃ grains.

The annealed MoO₃ thin layers deposited onto glass substrate showed a higher crystallinity grade especially for the 300 °C heat treated sample (see Figure 3a). It was calculated to 9.6% (on glass), in contrast to the 5.4% calculated crystallinity for the aluminum substrate-processed supported samples.

The average dislocation density and grain size of the MoO₃ films on glass substrate were estimated by the momentum method. In fact, inner stresses of the thin aluminum foil substrate were released via physical distortion such as bending and deflection during the heat treatment, resulting in the cracking of the MoO₃ thin film. Accordingly, the momentum method was applied for the crystalline sample prepared on the glass substrate. In fact, the momentum method was not applied in the case of the thin films prepared on aluminum substrate. The reason for this was due to the heat treatment of the thin films; the inner stresses of the thin aluminum foil substrate were released via physical distortion, namely, bending and deflection, so the thin film cracked on the surface of those. Since the momentum method is sensitive for such length scale-inducing effects and would not even correctly predict the average dislocation density, it cannot be used for the films on the aluminum substrate. However, in the case of glass substrate samples, coherent

results were obtained regarding the parameters from second and fourth-order restricted moments (Figure 3c, respectively Figure 3d.) The obtained average dislocation density $\langle \rho^* \rangle = 16 \times 10^{12} \text{ m}^{-2}$ and average dislocation cell size $d \approx 1.4$ are expected results for a partially recrystallized, fairly large, grained sample. In this case, we can assume that, truly, the average dislocation cell size is equivalent to the average grain size, because the obtained value is in the range of microns. However, this is not always true, because for extremely large-grained polycrystals (10–100 μm), the characteristic length of the dislocation structure will always be smaller than the size of the crystallites. Since the thin film has a thickness of 10–100 nm, the average grain size is obtained based on surface data, which means that the grains have a large anisotropic extent on the x-y plane in comparison to the z direction.

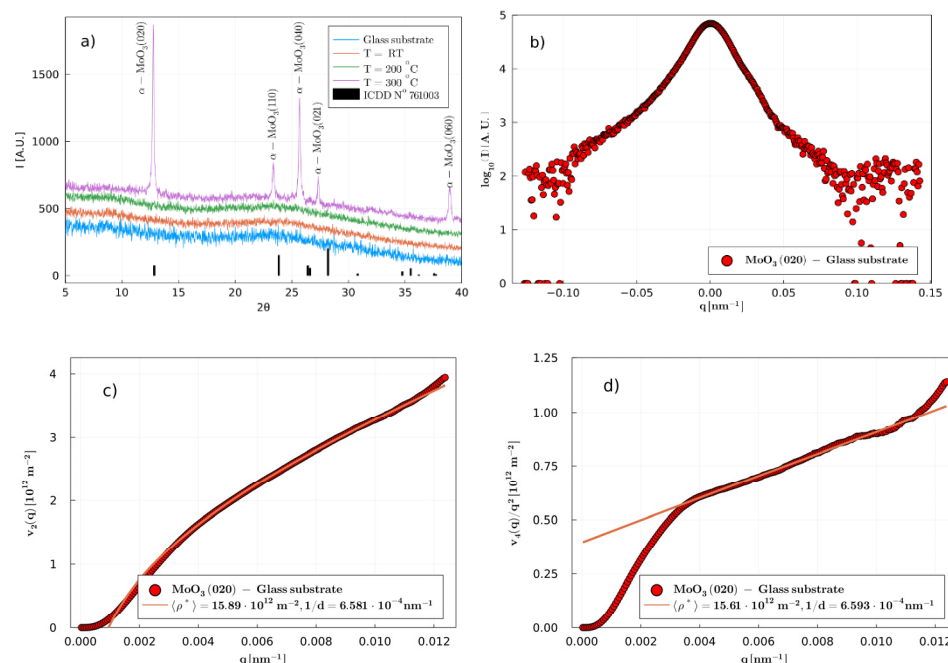


Figure 3. (a) XRD patterns of MoO₃ sputtered on glass substrate; (b) intensity distribution of the (200) Bragg-reflection; second-order (c) and fourth-order (d) restricted moments.

Mechanical hardness tests were performed on the thin layers sputtered on the aluminum substrate, which is the selected substrate that will serve later as the current collector for the MoO₃ cathodes in the thin-film Li-ion batteries. Six indentations were performed on each sample with different maximum applied forces up to $F = 40 \text{ mN}$. Figure 4a presents ones of the load vs. displacement curves for the three layers: as prepared, heat treated at 200 °C and 300 °C.

At first glance, it can be noted that the lowest maximum displacement recorded with the $F = 5 \text{ mN}$ load among the three different samples was found for the amorphous layer with penetration of 0.22 μm , followed by the layers heat treated at 200 °C and the 300 °C, with 0.3, and 0.7 μm respectively, which reflects the hardness conditions. Based on these three curves, we can conclude that the as-prepared and the 200 °C annealed samples have similar mechanical properties, unlike the 300 °C annealed one. As the indenter's tip penetrates the specimen, the loading curve raises. At some point, the maximum load P_{\max} is reached, which is then followed by the unloading.

The black and blue curves that belong to the as-prepared and 200 °C heat treated at 200 °C layers show the usual behavior of amorphous layers [40], which shows that the deformation was mostly determined by the amorphous phase even in the sample heat treated at 200 °C. In the case of the 300 °C-treated and thereby more crystallized layer (red curve), there were two main differences compared with the other samples. First, under a given load value, the indenter's tip can penetrate deeper into the sample,

which characterizes softer materials (Figure 5). Secondly, during the unloading part, the displacement did not decrease. This means that during the loading part, elastic energies do not accumulate and are stored in the material, only plastic deformation has occurred.

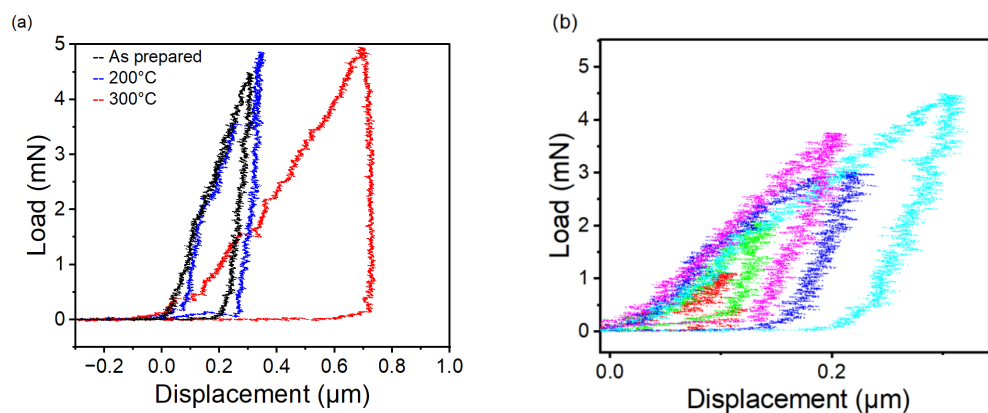


Figure 4. (a) Load vs. displacement curves at an $F = 5$ mN maximum load for the amorphous, 200 °C, and 300 °C annealed MoO_3 thin-film samples; (b) load vs. displacement curve for five indentations for the as-prepared sample.

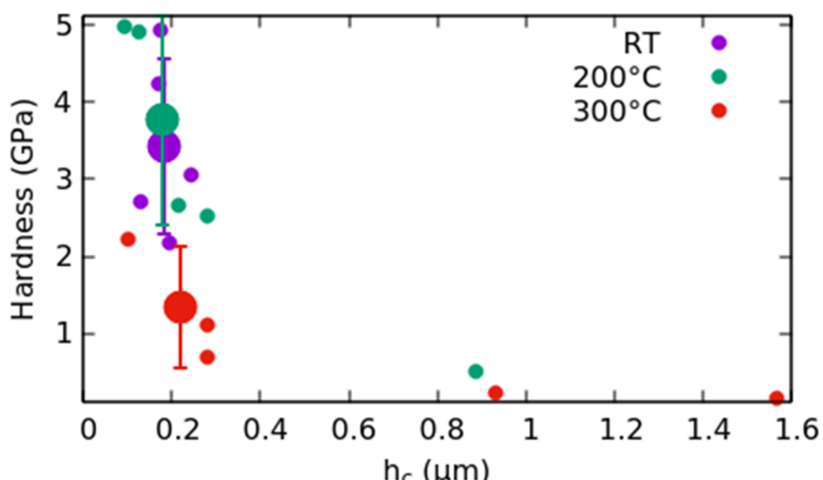


Figure 5. Hardness vs. contact surface depth after the total of 5 touches performed on each sample. The huge squares represent the average of the hardnesses whose displacements are below 0.4 um to eliminate the deterministic effect of the substrate.

During the loading phase of the as-prepared, amorphous layer, the load curve is continuous; there are no sudden jumps. This smooth curve behavior is linked to the deformation mechanism. In these cases, the deformation was homogeneous in space and time, and shows the elasticity storing capability of the amorphous phase. This can be also confirmed from the rest of the load vs. displacement curves of the as-prepared layer (Figure 4b) in five of the indentation curves present the same pattern.

The 300 °C heat-treated layer showed momentary jumps in the load vs. displacement graph. During these jumps a sudden plastic event occurred, where the load value remained close to constant, but the displacement had a sudden increase. These sudden deformation events could have more sources, such as the avalanche-like dislocation gliding and creeping, crack formation, and layer separation from its substrate. The possibility of these various and complex superposition-like deformation processes could serve as an explanation for the lack of the crystalline phase's elasticity.

The hardness H (GPa) depends on the maximum force P_{max} (mN) applied to the thin layers and the indentation depth (h_c (μm)) corresponding to the contact surface. Its value can be calculated from the following equation. The h_c can be determined by the point of intersection of the linear fitting to the first part of the unloading with the zero load the linear line x in the line projected to the initial values of the load curve [41].

$$H = \frac{P_{max}}{24.5 \times h_c^2} \quad (5)$$

Further investigations on the hardness (Figure 5) revealed that in the case of higher penetration than $0.4 \mu\text{m}$, the hardnesses were lower (around 300 MPa); these results were coming from the aluminum substrate and not the layer, as the penetration exceeded the layer thickness, which is in a good agreement with the expectation [42]. In order to have more accurate results of the hardness, all penetrations below $0.4 \mu\text{m}$ were averaged and presented with the larger circles.

Regarding the hardness of the MoO₃-bearing layers, there is a slight difference between the amorphous and the heat-treated sample at 200°C . The thin-film sample heat treated at 300°C is much softer than the previous ones due to its different deformation properties.

The indented layers were examined using scanning electron microscopy (SEM). Due to the semiconductive nature of MoO₃, the samples were carbon coated to a thickness of 7 nm as measured with a quartz crystal thickness gauge. The brittleness and the adhesion of the layers could be represented by the number of cracks. According to Figure 6a, the most elastic as-prepared layer shows the least number of cracks (as expected), followed by the heat-treated layer at 200°C , as presented in Figure 6b. The number of cracks is the highest for the 300°C layer (presented in cf. Figure 6c). In this figure, there is visible proof of the peeling of the layer from the substrate, which is in good agreement with the above section regarding the elastic conditions. This different peeling behavior was also expected. When a huge strain was applied on the substrate (caused by 40 mN load), the more elastic layer can follow better the deformation of the substrate and stay in contact.

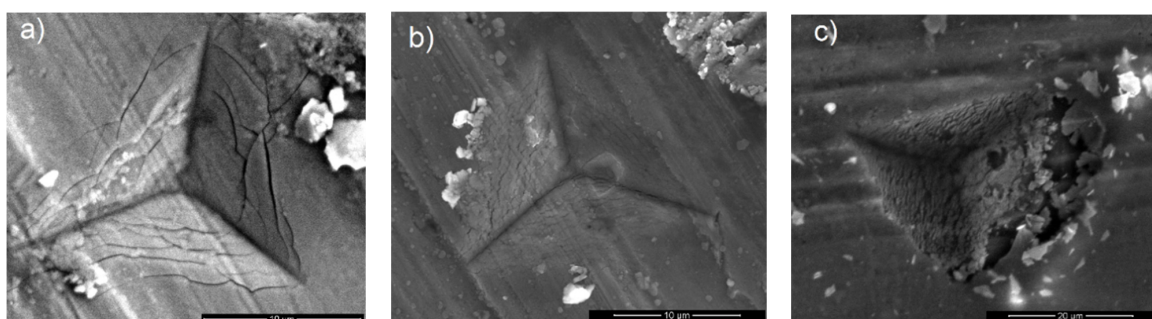


Figure 6. SEM images of 40 mN load effect on the layers (a) RT, (b) 200°C , and (c) 300°C .

Acoustic emission measurements were performed in parallel with the nanoindentation studies. Crack formation and its sudden propagation, or the cooperative motion of the dislocations in the layers during indentation can form a significant acoustic signal [39], while the slow deformation processes, such as the grain boundary sliding or the atomic rearrangement near local stress zones and free volumes (which characterize a common deformation process in amorphous materials [43]), produce no detectable acoustic signals.

This was in perfect agreement with the results obtained since the as-prepared layer did not produce any signals, while most of the acoustic emission signals were obtained from the samples heat treated at 200°C and 300°C . Altogether, four acoustic signals were detected during the six indentation runs from the samples heat treated at 200°C , and four acoustic signals in case of 300°C . The heat-treated samples are crystallized to some degree, but we cannot connect the AE signals clearly to the crystalline form, since there were no differences between the AE signals regarding the degree of crystallinity. Acoustic

signals may be generated from the cracks, and in the case of the 300 °C heat-treated 300 °C sample, the more cracks cannot produce more AE signals, because of the poorer adhesion of the layer.

The load and the amplitude of the acoustic emission signal are plotted as a function of the time during the indentation using a 10 mN maximum load (Figure 7). The detected AE signals were mostly in the loading part. In the fully crystalline most crystallized cases, there were AE signals during the unloading part (Figure 7b). This type of event was not unexpected in a rigid, totally plastic material, because it is shown in Figure 4a that during the unloading part, the tip's penetration could increase, so plastic deformation occurred. The lack of the AE events during the unloading part of the amorphous layers also shows that the leading deformation mechanism belongs to the amorphous parts. However, the existing AE signals of the 200 °C-treated layer show that there is some contribution of the substrate to the deformation mechanism.

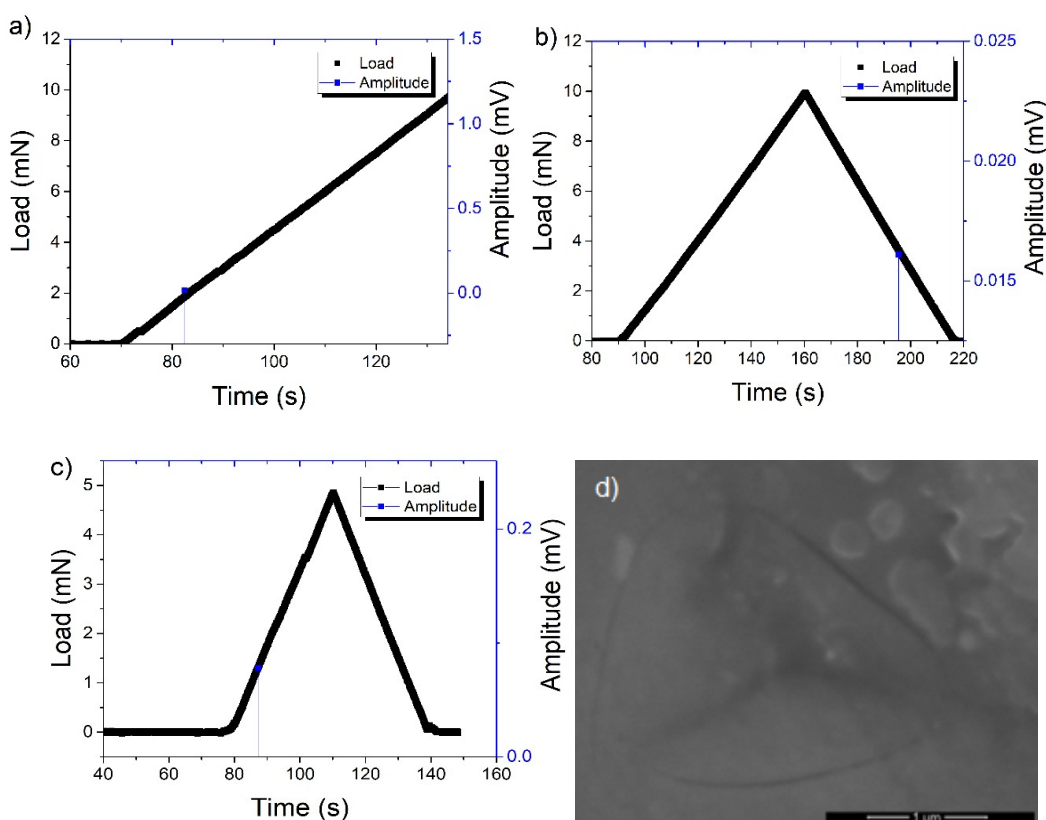


Figure 7. Load and acoustic emission amplitude signals as a function of time for the 10 mN indentation for the 200 °C layer and 300 °C layer (a) and (b), respectively. (c) Load and AE amplitude as a function of time for the 5 mN touch on the 200 °C MoO₃ layer; (d) SEM image of the crack after the indentation.

An interesting feature of the acoustic emission is that it can produce a signal after a crack as mentioned above. Figure 7c shows the acoustic emission signal during the loading phase; furthermore, the SEM image of the crack produced on the surface of the MoO₃ layer heat treated at 200 °C is shown in Figure 7d. It can be assumed that this crack formed at around F = 1.3 mN before the peeling out of the layer, since, during the crack formation, there was a good mechanical connection between the layer and the substrate, which makes it possible for the AE signal to propagate through the substrate to the detector from the crack in the layer.

In summary, the *as-prepared* MoO₃ layer has been proved to have the highest hardness and elasticity from the load–displacement curves. This higher elasticity was also proven by the fact that the *as-prepared* layer did not produce any acoustic emission signals. This means that

the main deformation mechanisms of the as-prepared layers are the acoustically silent atomic rearrangements. In these cases, the separation of the layer from the substrate is assumed to be the reason for the crack development or it occurred before the crack formation. The heat-treated layers, however, showed some jumps in the load–displacement curve; this can tell us about certain deformations/crack formation in the layer during the indentation, which is supported by the acoustic emission signals. It can be concluded that the main deformation mechanism was the cracking of the layer, which confirms their brittleness. From the SEM images of the indentation, it can be deduced that the heat treatment resulted in poor adhesion between the layer and the substrate, which could be due to the phase change from amorphous to crystalline. The use of the nanoindentation, acoustic emissions, and SEM images can tell us a lot about these properties of supported thin films.

To conclude this section, X-ray diffraction confirmed the amorphous nature of the as-sputtered MoO_3 thin films. According to surface mechanical studies, these films are adherent, hard, and elastic. As suggested by the XPS measurements, annealing of the films at 300 °C in air resulted in partial crystallization producing large grains elongated on the plane of the film. These films were rigid and brittle, with a tendency for peeling under mechanical stress. However, a significant amount of Mo-oxide remained in a disordered state even after this heat treatment. It can be assumed that the relatively large oxygen deficiency of the 300 °C annealed films, along with the increased Mo^{5+} content revealed by XPS, is related to the presence of this disordered fraction. Nevertheless, our results are consistent with the literature data suggesting the transition between amorphous and crystalline MoO_3 at around 300 °C [44,45]. Mechanical properties of the films annealed at 200 °C in air still show the prevalence of the amorphous oxide but are in some sense intermediate between those of the as-prepared and the 300 °C annealed systems. Although long-range ordered crystalline domains were not detected in these samples by XRD, their mechanical behavior, as well as slight changes in the Mo 3d XPS spectrum, is in line with the increasing local ordering.

(2) Electrochemical characterizations

The electrochemical cycling behaviors at $I = 25.25 \mu\text{A}$ charge/discharge currents of the battery cells assembled using the as-sputtered, 200 °C and 300 °C heat-treated samples are depicted in Figure 8. The charge–discharge curve consists of smooth S-shape profiles at any cycle without having a flat plateau average voltage of about 1.9 V. As shown in Figure 8a,b for the as-sputtered and the 200 °C heat-treated samples, a rather high initial irreversible capacity was observed, which was smaller in the case of the sample heat treated at 300 °C (cf. Figure 8c). In fact, the as-sputtered cell showed the highest initial capacity of around 50 μAh compared to 44 μAh for 200 °C and 35 μAh for the electrode heat treated at 300 °C. On the other hand, the best coulombic efficiency (Figure 9a) was for the 300 °C heat-treated layer at 300 °C followed by the 200 °C heat-treated layer at 200 °C and, finally, the as-prepared layer.

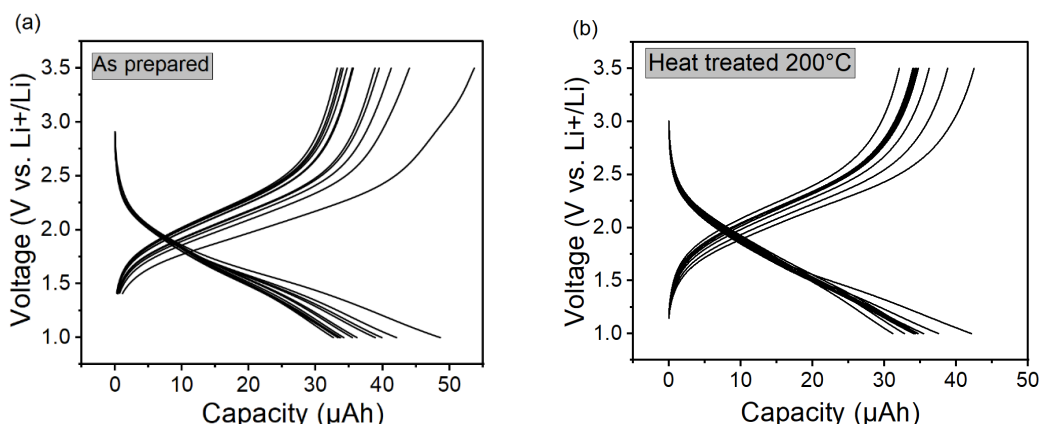


Figure 8. Cont.

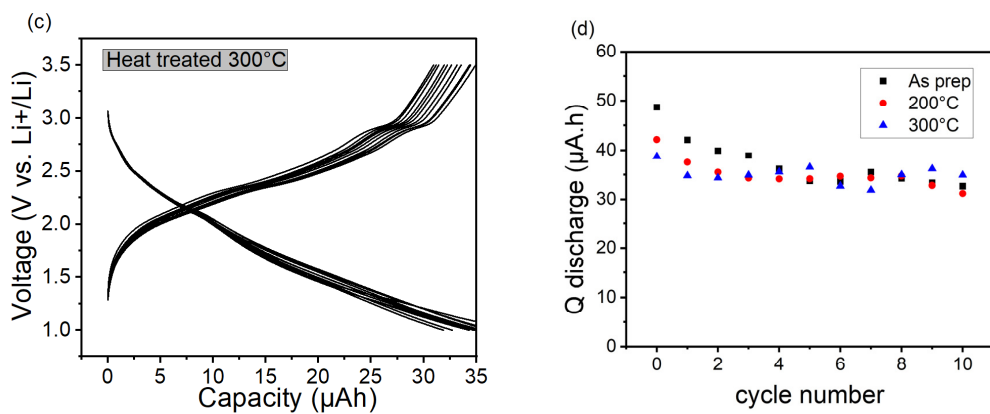


Figure 8. The Charge and Discharge Voltage Profiles (a) as-prepared, (b) heat treated at 200 °C, (c) heat treated at 300 °C, (d) discharge capacity vs. cycle number after 10 cycles at 0.5 C rate; the arrow in the figures shows the change from 1st cycle until the 10th moving from right to left.

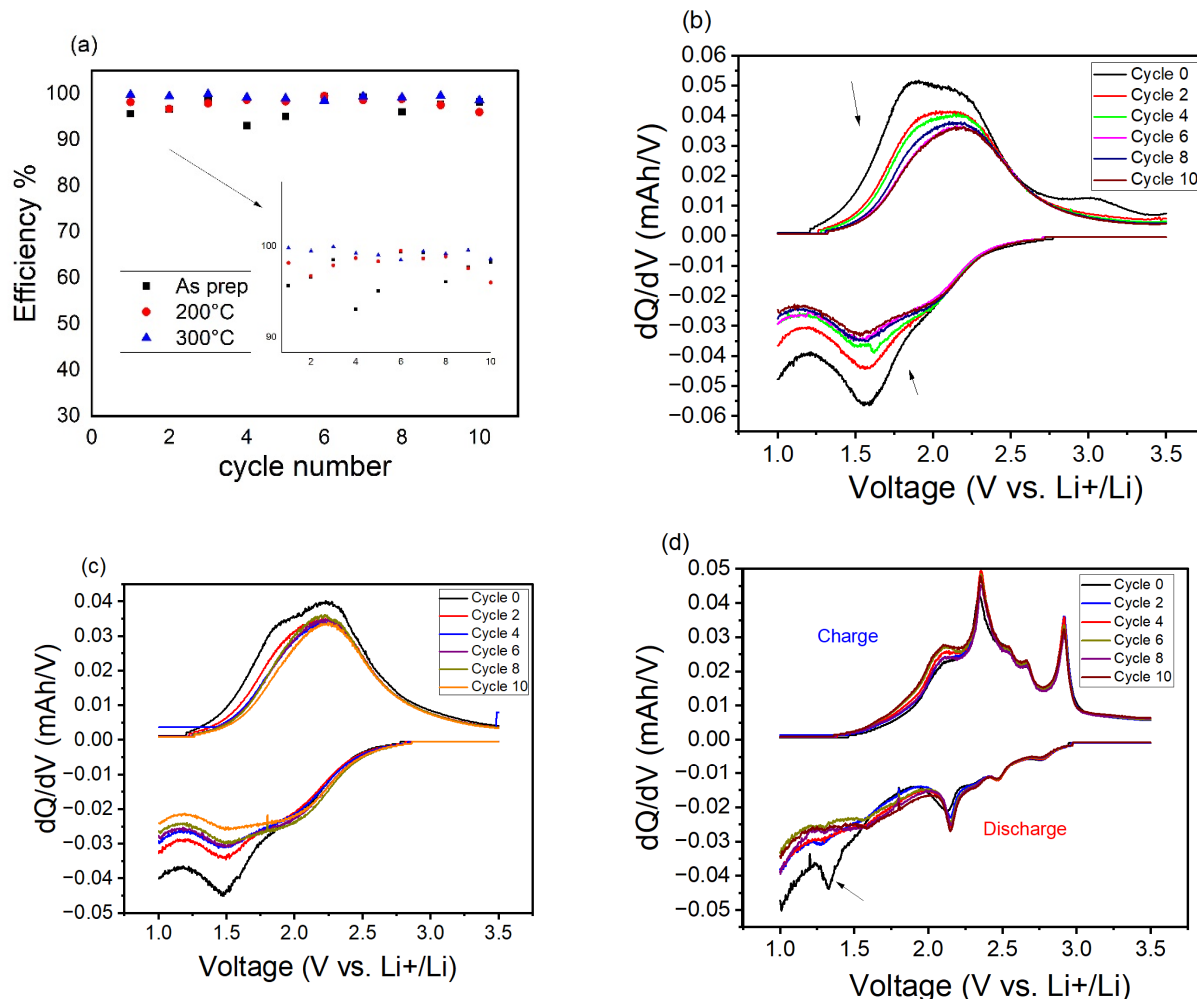


Figure 9. Coulombic efficiency (a), Differential capacity graphs of the 3 cells after 10 cycles: (b) as-prepared, (c) heat-treated 200 °C, (d) heat-treated 300 °C.

In terms of coulombic efficiency (Figure 9a), the heat-treated layer at 300 °C showed superiority compared to the layer heat treated at 200 °C and the as-prepared amorphous layer.

Differential capacity curves of MoO₃ electrodes heat treated at different temperatures are shown in Figure 9b–d. In Figure 9b, the charge branches (positive current values) of

the cycling data show a broadened character without sharp signal peaks, which may be attributed to the amorphous nature of the applied cathode material and the broad energy distribution of the reaction sites in the electrode active material [19].

Compared to the as-prepared electrode layer, the electrode layer treated at 200 °C shows similar electrochemical behaviors, which can be explained by the similar, predominantly amorphous structural features discussed above. The as-prepared and the 200 °C-treated electrode layers are rather amorphous and therefore similar electrochemical performance is expected. In fact, the electrode layer treated at 300 °C shows remarkably different electrochemical behavior than the previous ones. Sharper and more intense peaks compared to the amorphous and the 200 °C layer can be observed on its incremental capacity curves (charge and discharge, cf. Figure 9c,d), and this could be correlated to the crystal phase structure of the electrode, as previously confirmed with the XRD analyses, i.e., the heat treatment at 300 °C led to the partial crystallization of the MoO₃ layer. The 300 °C heat-treated MoO₃ layer presented in the differential capacity curve (Figure 9d) exhibits two strong peaks at 2.4 V and 3 V, observed during the charging process, and two reversible signals at 2.2 V and 2.6V during discharge, while a peak at 1.4V arises due to an irreversible electrochemical process; its intensity diminishes with the consecutive cycles.

The multiple peaks during charge/discharge for the layer heat treated at 300 °C can be explained by its partial crystallization; in other words, Li⁺ was inserted into both the crystalline and amorphous sites. Since orthorhombic MoO₃ possesses a layered structure, the peaks at 3V/2.2V, which are in perfect agreement with the literature [46,47], can be attributed to the insertion/extraction of Li⁺ ions in the interlayers of the crystalline MoO₃, while the rest of the peaks are assumed to be part of the insertion/extraction of Li⁺ ions in the amorphous regions of the thin layer.

The as-prepared layer showed good stability throughout the 500 full cycles compared to the heat-treated layer at 200 °C and more specifically to the layer treated at 300 °C, which experienced a significant capacity loss and eventually a cell failure after reaching 160 cycles (see Figure 10). This cell failure was expected, and it is in accordance with the nanoindentation and SEM results that indicate the more brittle structure of the crystalline layer, which is more prone to the electrochemically induced internal stresses and the concomitant delamination and detachment from the metallic current collector, which is assumed based on the nanoindentation and hardness analysis mentioned above. Amorphous MoO₃ shows increased cycling stability, although with less defined electrochemical features, which is in accordance with previous publications [47].

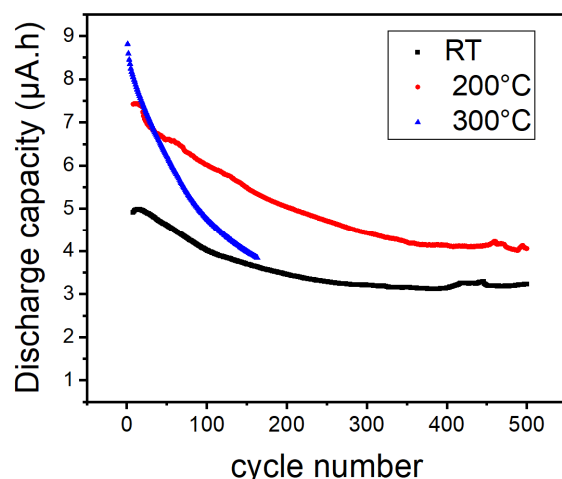


Figure 10. Capacity vs. cycle number after 500 cycles at 10 C rate of the three differently treated MoO₃ electrode layers.

3. Conclusions

In the present work, the structural, nanomechanical, and electrochemical characteristics of amorphous and crystalline MoO_3 thin layers designed for use in rechargeable Li-ion batteries as their positive electrodes were studied. The as-prepared amorphous layer showed superior electrochemical performance in terms of higher capacity and longer-term cycling stability compared to the layer heat treated at 200 °C and especially the layer heat treated at 300 °C. This superiority is directly correlated to the crystal structure and the nanomechanical properties of the layers, the XRD results revealed that the as-prepared layer was rather predominantly amorphous along with the layer, similar to the one heat treated at 200 °C, whereas the layer heat treated at 300 °C was partially crystalline showing the orthorhombic MoO_3 phase. The layers were then analyzed via nanoindentation coupled with acoustic emissions, indicating that the as-prepared (amorphous) film was the most elastic and adherent; when testing their mechanical properties, the highest flexibility belonged to the as-prepared film followed by the layer annealed at 200 °C, while the least flexible and most brittle layer was the 300 °C heat-treated sample. The tendency for cracking and delamination of the 300 °C heat-treated film was confirmed in order to have a better understanding of the impact left after the nanoindentation and images of the layers. SEM analysis was used through which it was confirmed that the layers heat treated at 300 °C possessed numerous cracks compared to the other layers; thus, the highest brittleness. Eventually, it was concluded that crystallinity has, on one hand, a positive effect on the initial irreversible capacity losses during the battery cell formation period; on the other hand, it has a negative effect on the cycle-life performance, due to its lesser durability against the prolonged electrochemical lithium de-/insertion-induced electro-chemo-mechanical processes. Moreover, it is assumed that its power density performance may be inferior, caused by the significantly higher electronic resistivity of the cathode layers caused by the grain boundaries in the more crystallized sputtered thin-film cathodes.

Author Contributions: Conceptualization, R.K.; methodology, R.K., I.G., P.J., Z.D.; investigation, W.M., S.L., D.U., Z.P.; writing—original draft preparation, W.M., E.P., R.K.; writing—review and editing, W.M. and R.K.; project administration, R.K.; funding acquisition, R.K. All authors have read and agreed to the published version of the manuscript.

Funding: Project no. K_134696 was implemented with the support provided by the Ministry of Innovation and Technology of Hungary from the National Research, Development, and Innovation Fund, (NRDIO) financed under the OTKA K_20 funding scheme.

Institutional Review Board Statement: Not applicable.

Informed Consent Statement: Not applicable.

Data Availability Statement: Data is available upon request sent to the corresponding author.

Conflicts of Interest: The authors declare no conflict of interest.

References

- Yada, C.; Iriyama, Y.; Jeong, S.-K.; Abe, T.; Inaba, M.; Ogumi, Z. Electrochemical properties of LiFePO_4 thin films prepared by pulsed laser deposition. *J. Power Sources* **2005**, *146*, 559–564. [[CrossRef](#)]
- Strauß, F.; Hüger, E.; Heitjans, P.; Trouillet, V.; Bruns, M.; Schmidt, H. Li-Si thin films for battery applications produced by ion-beam co-sputtering. *RSC Adv.* **2014**, *5*, 7192–7195. [[CrossRef](#)]
- Ahn, D.; Kim, C.; Lee, J.-G.; Park, B. The effect of nitrogen on the cycling performance in thin-film $\text{Si}_{1-x}\text{N}_x$ anode. *J. Solid State Chem.* **2008**, *181*, 2139–2142. [[CrossRef](#)]
- Yamada, I.; Abe, T.; Iriyama, Y.; Ogumi, Z. Lithium-ion transfer at LiMn_2O_4 thin film electrode prepared by pulsed laser deposition. *Electrochim. Commun.* **2003**, *5*, 502–505. [[CrossRef](#)]
- Morales, J.; Sánchez, L.; Martín, F.; Ramos-Barrado, J.R.; Sánchez, M. Nanostructured CuO thin film electrodes prepared by spray pyrolysis: A simple method for enhancing the electrochemical performance of CuO in lithium cells. *Electrochim. Acta* **2004**, *49*, 4589–4597. [[CrossRef](#)]
- Julien, C.; Nazri, G.; Guesdon, J.; Gorenstein, A.; Khelfa, A.; Hussain, O. Influence of the growth conditions on electrochemical features of MoO_3 film-cathodes in lithium microbatteries. *Solid State Ion.* **1994**, *73*, 319–326. [[CrossRef](#)]

7. Chou, S.-L.; Wang, J.-Z.; Liu, H.-K.; Dou, S.-X. Electrochemical deposition of porous Co_3O_4 nanostructured thin film for lithium-ion battery. *J. Power Sources* **2008**, *182*, 359–364. [[CrossRef](#)]
8. Glenneberg, J.; Andre, F.; Bardenhagen, I.; Langer, F.; Schwenzel, J.; Kun, R. A concept for direct deposition of thin film batteries on flexible polymer substrate. *J. Power Sources* **2016**, *324*, 722–728. [[CrossRef](#)]
9. Gockeln, M.; Glenneberg, J.; Busse, M.; Pokhrel, S.; Mädler, L.; Kun, R. Flame aerosol deposited $\text{Li}_4\text{Ti}_5\text{O}_{12}$ layers for flexible, thin film all-solid-state Li-ion batteries. *Nano Energy* **2018**, *49*, 564–573. [[CrossRef](#)]
10. Julien, C.M.; Mauger, A. Pulsed laser deposited films for microbatteries. *Coatings* **2019**, *9*, 386. [[CrossRef](#)]
11. Xiong, F.; Tao, H.; Yue, Y. Role of Amorphous Phases in Enhancing Performances of Electrode Materials for Alkali Ion Batteries. *Front. Mater.* **2020**, *6*, 328. [[CrossRef](#)]
12. Kanazawa, S.; Baba, T.; Yoneda, K.; Mizuhata, M.; Kanno, I. Deposition and performance of all solid-state thin-film lithium-ion batteries composed of amorphous Si/LiPON/VO-LiPO multilayers. *Thin Solid Films* **2020**, *697*, 137840. [[CrossRef](#)]
13. Kim, K.H.; Iriyama, Y.; Yamamoto, K.; Kumazaki, S.; Asaka, T.; Tanabe, K.; Fisher, C.A.; Hirayama, T.; Murugan, R.; Ogumi, Z. Characterization of the interface between LiCoO_2 and $\text{Li}_7\text{La}_3\text{Zr}_2\text{O}_{12}$ in an all-solid-state rechargeable lithium battery. *J. Power Sources* **2011**, *196*, 764–767. [[CrossRef](#)]
14. Lee, Y.M.; Lee, J.; Shim, H.-T.; Lee, J.K.; Park, J.-K. SEI Layer Formation on Amorphous Si Thin Electrode during Precycling. *J. Electrochem. Soc.* **2007**, *154*, A515–A519. [[CrossRef](#)]
15. Mattelaer, F.; Geryl, K.; Rampelberg, G.; Dendooven, J.; Detavernier, C. Amorphous and Crystalline Vanadium Oxides as High-Energy and High-Power Cathodes for Three-Dimensional Thin-Film Lithium Ion Batteries. *ACS Appl. Mater. Interfaces* **2017**, *9*, 13121–13131. [[CrossRef](#)]
16. Zhou, T.; Zheng, Y.; Gao, H.; Min, S.; Li, S.; Liu, H.K.; Guo, Z. Surface Engineering and Design Strategy for Surface-Amorphized $\text{TiO}_2@\text{Graphene}$ Hybrids for High Power Li-Ion Battery Electrodes. *Adv. Sci.* **2015**, *2*, 1500027. [[CrossRef](#)]
17. Julien, C.; Nazri, G.A. Solid State Batteries: Materials Design and Optimization. In *BT-Electronic Materials: Science and Technology*; Springer Science & Business Media: Berlin, Germany, 1994; p. 1995.
18. Ku, J.H.; Ryu, J.H.; Kim, S.H.; Han, O.H.; Oh, S.M. Reversible lithium storage with high mobility at structural defects in amorphous molybdenum dioxide electrode. *Adv. Funct. Mater.* **2012**, *22*, 3658–3664. [[CrossRef](#)]
19. Liu, C.; Neale, Z.G.; Cao, G. Understanding electrochemical potentials of cathode materials in rechargeable batteries. *Mater. Today* **2016**, *19*, 109–123. [[CrossRef](#)]
20. Chae, O.B.; Kim, J.; Park, I.; Jeong, H.; Ku, J.H.; Ryu, J.H.; Kang, K.; Oh, S.M. Reversible lithium storage at highly populated vacant sites in an amorphous vanadium pentoxide electrode. *Chem. Mater.* **2014**, *26*, 5874–5881. [[CrossRef](#)]
21. Chen, W.; Zhang, H.; Wang, Y.; Ma, Z.; Li, Z. In-situ microstructural investigations by electron-beam irradiation induced crystallization of amorphous moo_x thin films with high performance for li-ion storage. *Electrochim. Acta* **2014**, *144*, 369–375. [[CrossRef](#)]
22. Icovici, M.; Panero, S.; D’Agate, A.; Pistoia, G.; Temperoni, C. Non-stoichiometric molybdenum oxides as cathodes for lithium cells. Part II. Secondary batteries. *J. Electroanal. Chem. Interfacial Electrochem.* **1979**, *102*, 343–349. [[CrossRef](#)]
23. Swiatowska-Mrowiecka, J.; de Diesbach, S.; Maurice, V.; Zanna, S.; Klein, L.; Briand, E.; Vickridge, I.; Marcus, P. Li-Ion Intercalation in Thermal Oxide Thin Films of MoO_3 as Studied by XPS, RBS, and NRA. *J. Phys. Chem. C* **2008**, *112*, 11050–11058. [[CrossRef](#)]
24. Ahmed, B.; Shahid, M.; Nagaraju, D.H.; Anjum, D.H.; Hedhili, M.N.; Alshareef, H.N. Surface Passivation of MoO_3 Nanorods by Atomic Layer Deposition toward High Rate Durable Li Ion Battery Anodes. *ACS Appl. Mater. Interfaces* **2015**, *7*, 13154–13163. [[CrossRef](#)] [[PubMed](#)]
25. Mariotti, D.; Lindström, H.; Bose, A.C.; Ostrikov, K. Monoclinic β - MoO_3 nanosheets produced by atmospheric microplasma: Application to lithium-ion batteries. *Nanotechnology* **2008**, *19*, 495302. [[CrossRef](#)] [[PubMed](#)]
26. Fjellvåg, S.; Ruud, A.; Sønsteby, H.H.; Nilsen, O.; Fjellvåg, H. Crystallization, Phase Stability, and Electrochemical Performance of β - MoO_3 Thin Films. *Cryst. Growth Des.* **2020**, *20*, 3861–3866. [[CrossRef](#)]
27. Julien, C.; Nazri, G. Transport properties of lithium-intercalated MoO_3 . *Solid State Ion.* **1994**, *68*, 111–116. [[CrossRef](#)]
28. Yebka, B.; Julien, C. Lithium intercalation in sputtered MoO_3 films. *Ionic* **1997**, *3*, 83–88. [[CrossRef](#)]
29. Fairley, N., CasaXPS: Spectrum Processing Software...Google Scholar. Available online: https://scholar.google.com/scholar?hl=en&as_sdt=0%2C5&q=Fairley%2C+N%2C+CasaXPS%3A+Spectrum+Processing+Software+for+XPS%2C+AES+and+SIMS%2C+Version+2.3.13%2C+Casa+Software+Ltd%2C+Cheshire%2C+2006+http%3A%2F%2Fwww.casaxps.com&bttG= (accessed on 2 February 2022).
30. Mohai, M. XPS MultiQuant: Multimodel XPS quantification software. *Surf. Interface Anal.* **2004**, *36*, 828–832. [[CrossRef](#)]
31. Baltrusaitis, J.; Mendoza-Sanchez, B.; Fernandez, V.; Veenstra, R.; Dukstiene, N.; Roberts, A.; Fairley, N. Generalized molybdenum oxide surface chemical state XPS determination via informed amorphous sample model. *Appl. Surf. Sci.* **2015**, *326*, 151–161. [[CrossRef](#)]
32. Scanlon, D.O.; Watson, G.W.; Payne, D.J.; Atkinson, G.R.; Egddell, R.G.; Law, D.S.L. Theoretical and experimental study of the electronic structures of MoO_3 and MoO_2 . *J. Phys. Chem. C-Condens. Matter Mater. Phys.* **2010**, *114*, 4636–4645. [[CrossRef](#)]
33. Groma, I. X-ray line broadening due to an inhomogeneous dislocation distribution. *Phys. Rev. B* **1998**, *57*, 7535–7542. [[CrossRef](#)]
34. Borbély, A.; Groma, I. Variance method for the evaluation of particle size and dislocation density from x-ray Bragg peaks. *Appl. Phys. Lett.* **2001**, *79*, 1772–1774. [[CrossRef](#)]

35. Groma, I.; Székely, F. Analysis of the asymptotic properties of X-ray line broadening caused by dislocations. *J. Appl. Crystallogr.* **2000**, *33*, 1329–1334. [[CrossRef](#)]
36. Hegyi, I.; Ispánovity, P.D.; Knapek, M.; Tüzes, D.; Máthis, K.; Chmelík, F.; Dankházi, Z.; Varga, G.; Groma, I. Micron-scale deformation: A coupled in situ study of strain bursts and acoustic emission. *Microsc. Microanal.* **2017**, *23*, 1076–1081. [[CrossRef](#)]
37. Ispánovity, P.D.; Ugi, D.; Péterffy, G.; Knapek, M.; Kalácska, S.; Tüzes, D.; Dankházi, Z.; Máthis, K.; Chmelík, F.; Groma, I. Dislocation avalanches are like earthquakes on the micron scale. *Nat. Commun.* **2022**, *13*, 1–10. [[CrossRef](#)]
38. Scruby, C.B. An Introduction to Acoustic Emission. *J. Phys. E Sci. Instrum.* **1987**, *20*, 946. [[CrossRef](#)]
39. Sikorski, W. *Acoustic Emission*; IntechOpen: London, UK, 2012.
40. Li, X.; Diao, D.; Bhushan, B. Fracture mechanisms of thin amorphous carbon films in nanoindentation. *Acta Mater.* **1997**, *45*, 4453–4461. [[CrossRef](#)]
41. Oliver, W.C.; Pharr, G.M. An improved technique for determining hardness and elastic modulus using load and displacement sensing indentation experiments. *J. Mater. Res.* **1992**, *7*, 1564–1583. [[CrossRef](#)]
42. Volinsky, A.; Vella, J.; Adhiketty, I.; Saruhan, V.; Mercado, L.; Yeung, B.; Gerberich, W. Microstructure and mechanical properties of electroplated Cu thin films. *MRS Online Proc. Libr. (OPL)* **2000**, *649*, Q5.3.1–Q5.3.6. [[CrossRef](#)]
43. Argon, A.S. Plastic deformation in metallic glasses. *Acta Metall.* **1979**, *27*, 47–58. [[CrossRef](#)]
44. McEvoy, T.M.; Stevenson, K.J.; Hupp, J.T.; Dang, X. Electrochemical preparation of molybdenum trioxide thin films: Effect of sintering on electrochromic and electroinsertion properties. *Langmuir* **2003**, *19*, 4316–4326. [[CrossRef](#)]
45. Cauduro, A.L.F.; Dos Reis, R.; Chen, G.; Schmid, A.K.; Méthivier, C.; Rubahn, H.-G.; Bossard-Giannesini, L.; Cruguel, H.; Witkowski, N.; Madsen, M. Crystalline Molybdenum Oxide Thin-Films for Application as Interfacial Layers in Optoelectronic Devices. *ACS Appl. Mater. Interfaces* **2017**, *9*, 7717–7724. [[CrossRef](#)] [[PubMed](#)]
46. Wen, Z.; Wang, Q.; Li, J. Electrochemical behavior of α -MoO₃ nanorods as cathode materials for rechargeable lithium batteries. *J. Nanosci. Nanotechnol.* **2006**, *6*, 2117–2122. [[CrossRef](#)]
47. Phuruangrat, A.; Chen, J.S.; Lou, X.W.; Yayapao, O.; Thongtem, S.; Thongtem, T. Hydrothermal synthesis and electrochemical properties of α -MoO₃ nanobelts used as cathode materials for Li-ion batteries. *Appl. Phys. A Mater. Sci. Process.* **2012**, *107*, 249–254. [[CrossRef](#)]